DE GRUYTER Nanophotonics 2021; 10(16): 4019–4026

Research Article

Zhen Jiang, Yizhou Ding, Chaoxiang Xi, Guangqiang He* and Chun Jiang*

Topological protection of continuous frequency entangled biphoton states

https://doi.org/10.1515/nanoph-2021-0371
Received July 13, 2021; accepted October 18, 2021;

Abstract: Topological quantum optics that manipulates the topological protection of quantum states has attracted special interests in recent years. Here we demonstrate valley photonic crystals implementing topologically protected transport of the continuous frequency entangled biphoton states. We numerically simulate the nonlinear four-wave mixing interaction of topological valley kink states propagating along the interface between two valley photonic crystals. We theoretically clarify that the signal and idler photons generated from the four-wave mixing interaction are continuous frequency entangled. The numerical simulation results imply that the entangled biphoton states are robust against the sharp bends and scattering, giving clear evidence of topological protection of entangled photon pairs. Our proposal paves a concrete way to perform topological protection of entangled quantum states operating at telecommunication wavelengths.

Keywords: quantum entanglement; topological photonics; valley photonic crystals.

1 Introduction

Topological insulators, striking paradigms that implement the insulating bulk, and conducting edge, have prompted the contexts of condensed matter physics. Photonic analog of topological insulators emulating quantum Hall effect in two-dimensional (2D) photonic systems were first demonstrated by Haldane and Raghu [1, 2]. Topological insulators embedding the breaking of time-reversal symmetry require the application of static or synthetic magnetic fields. Subsequently, a profound topological model preserving time-reversal symmetry which is identified by quantum spin Hall (QSH) insulators has been employed [3–5] in photonic systems. Photonic QSH insulators that support topologically protected edge states at the interface between two distinct topologies have been manipulated either theoretically or experimentally [6–8]. Recent researches have exploited [9–12] a new concept of topological phases, referring to the quantum valley Hall (QVH) effect. Valley pseudospins, recognized as a degree of freedom, is a promising platform to realize topologically protected transport in photonic devices. It has been experimentally implemented [13–17] that topological kink states can be conducted at the interface between regions with two distinct valley topologies. The valley kink states show topological nontrivial performances such as back-scattering suppression and robustness against imperfections and disorders.

Inspired by advanced behaviors of topological protection, researchers are focusing on exploiting the concepts of topology in the fields of nonlinear and quantum optics. Topological physics provides new exciting aspects of nonlinear optics. For instance, topological protected third-harmonic generation has been experimentally realized [18] in photonic topological metasurfaces emulating the QSH effect. Moreover, a configuration of the graphene metasurface imitating the quantum Hall effect theoretically proves [19] that the four-wave mixing (FWM) is topologically protected with the breaking of time-reversal symmetry. Most recently, the combination of topological edge states and quantum optics gives rise to potential applications for quantum communication, such as a topological quantum source [20], topological single quantum emitters [21], topological biphoton quantum states [22, 23], topologically protected quantum interference [24], and even quantum entanglement [25]. The aforementioned nonlinear and topological quantum photonic devices may provide a manipulated platform for on-chip nonlinear manipulation or quantum information processing.

Here we demonstrate topologically protected entangled biphoton states generated from the nonlinear spontaneous

---

***Corresponding authors: Guangqiang He and Chun Jiang**, State Key Laboratory of Advanced Optical Communication Systems and Networks, Shanghai Jiao Tong University, Shanghai 20040, China, E-mail: gqhe@sjtu.edu.cn (G. He), cjiang@sjtu.edu.cn (C. Jiang). https://orcid.org/0000-0001-9017-4159 (G. He)
Zhen Jiang, Yizhou Ding and Chaoxiang Xi, State Key Laboratory of Advanced Optical Communication Systems and Networks, Shanghai Jiao Tong University, Shanghai 20040, China

FWM process in photonic crystals emulating the QVH effect. We exploit the linear dispersion relations of valley kink states and explore the transmittances of kink states in the valley photonic crystals (VPCs). Idler photons generated from the FWM process propagating along the topological interfaces are observed due to the emergence of the nonlinear FWM interaction in the configurations. We theoretically clarify the continuous frequency entanglement of generated photon pairs. Quantum optical properties such as the joint spectral amplitude (JSA), Schmidt coefficients, and the entropy of entanglement for biphoton states generated in VPC waveguides are calculated. A remarkable motivation for transferring topological protection into quantum optics is to implement topologically protected quantum states. We numerically simulate the robustness of entangled biphoton states propagating along the interface with sharp bends. The results reveal that edge states of the pump, signal and idler are robust to the sharp bends due to the overlap between the frequencies of FWM interactions and operation bandwidths of valley kink states. The photonic systems supporting topologically protected entangled photon pairs may provide a prospective paradigm for guiding quantum information in on-chip quantum photonics.

2 Results

2.1 Topological VPCs

With the advent of all-dielectric VPCs, topological valley kink states become a practical way to protect nonlinear FWM processes in on-chip valley Hall topological insulators. We demonstrate a scheme of silicon-based VPCs implementing robust one-way light transport along the topological interface, as shown in Figure 1(a). The photonic design comprises equilateral triangular nanoholes with honeycomb lattices possessing C_6 symmetry. With the excitation of the source at the pump frequency ω_p, a

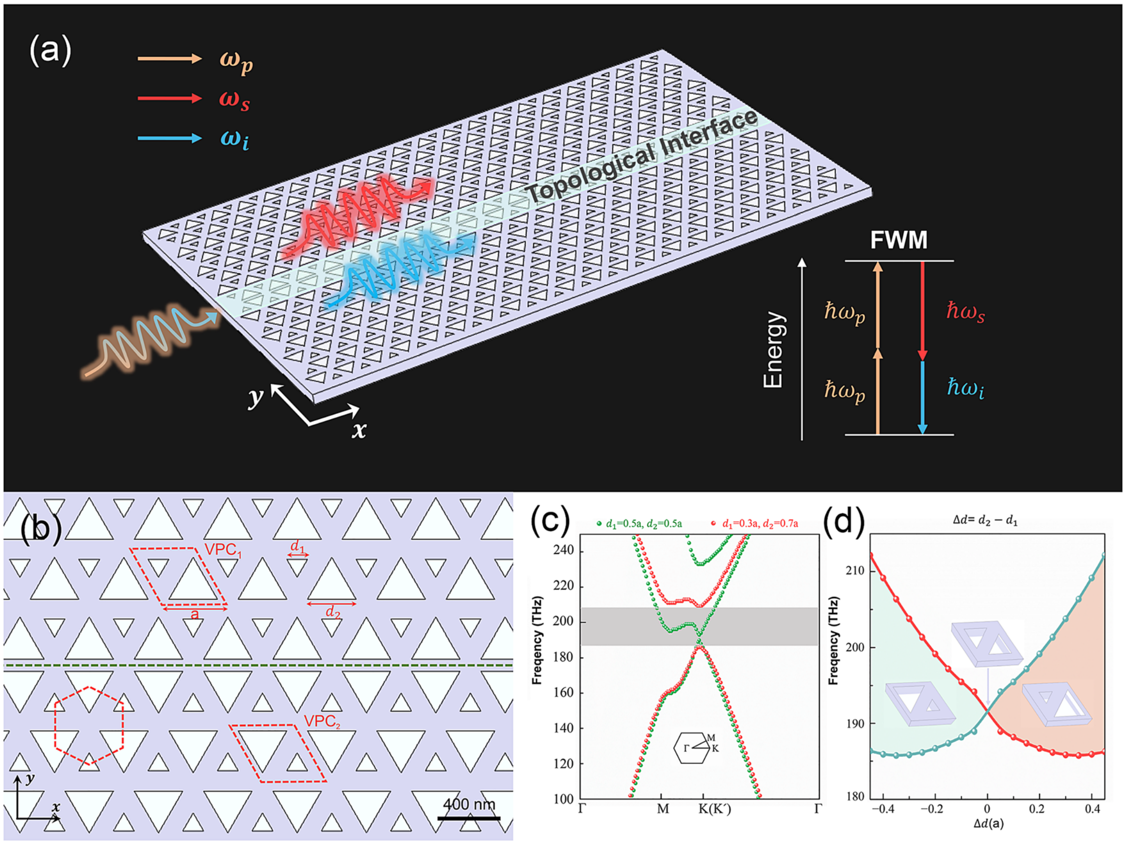

Figure 1: Diagram of the on-chip VPC topological insulators.
(a) Geometry of silicon-based VPCs implementing topological valley kink states, the inset shows energy conversion of nonlinear FWM process. (b) 2D close-up image of VPCs with lattice constant $a = 410$ nm, green dashed line denotes the interface between VPC$_1$ ($d_1 = 0.3a$, $d_2 = 0.7a$) and VPC$_2$ ($d_1 = 0.7a$, $d_2 = 0.3a$). (c) Corresponding band structures of VPC where the green and red dots represent the band of ordinary unit cells ($d_1 = d_2 = 0.5a$) and deformed unit cells ($d_1 = 0.3a$, $d_2 = 0.7a$), respectively. (d) Diagram of the topological bandgap of VPCs as a function of Δd ($\Delta d = d_1 - d_2$).

nonlinear spontaneous FWM process emerges due to the intrinsic third-order nonlinearity of silicon, leading to the generation of correlated signal and idler photons which correspond to the angular frequencies ω_s and ω_i, respectively. As described in the inset, the energy conversion of the FWM processes satisfies $2\hbar\omega_p = \hbar\omega_s + \hbar\omega_i$. With optimized parameters of VPCs, the frequencies of pump, signal and idler photons are all localized inside the operation bandwidth of topological valley kink states. Topological protected transport of pump, signal and idler photons can be manipulated along the topological interface.

We first study the linear topological nature of VPCs, as depicted in Figure 1(b), the 2D close-up image of proposed scheme is composed of two different VPCs with parity-inversed lattices, referred to as VPC_1 and VPC_2. The lattice constant of each unit cell is regarded as a, nano hole sizes are defined as d_1 and d_2, respectively. The corresponding band structure of VPC is plotted in Figure 1(c), for ordinary unit cells ($d_1 = d_2 = 0.5a$), there exist degenerate Dirac cones (at the K and K$'$ valleys) due to the C_6 lattice symmetry, as displayed by green dots in Figure 1(c). With the deformation of the unit cell ($d_1 = 0.3a$, $d_2 = 0.7a$), the C_6 lattice symmetry of VPC reduces to C_3 lattice symmetry, leading to the emergence of a topological photonic bandgap at the K (K$'$) point in the first Brillouin zone [16], as illustrated by red dots in Figure 1(c). By calculating the integration of Berry curvatures over the Brillouin zone, the valley Chern numbers of VPCs are given by $C_{K/K'} = \pm 1/2$ [9, 10, 15, 16]. Therefore, the valley Chern number of the system composed of VPC_1 and VPC_2 is calculated as $|C_{K/K'}| = 1$, resulting in topological nontrivial nature of VPCs [15, 16]. To quantitatively analyze the topological transition of VPCs, we simulate the evolution of bandgap of VPC with the function of Δd ($\Delta d = d_1 - d_2$), as visualized in Figure 1(d). Notably, the sizes of bandgaps grow with the increasing of Δd.

2.2 Linear response of topological valley kink states

To get more insight into the underlying features of topological valley kink states, we calculate the dispersion relation of the configuration comprising of VPC_1 and VPC_2 (Figure 2(a)). As illustrated in Figure 2(c), there exists a pair of valley-dependent edge modes localized inside the topological bandgap, and the dispersion curves with opposite slopes indicates the opposite propagation directions of two kink states. In other words, the propagating direction of kink states locks to valleys, which refers to as "valley-locked" chirality [26]. Noticeably, the dispersion slope is virtually linear, which provides a convenient method to design the nonlinear spontaneous FWM process. For pragmatic consideration, we choose pump frequency $\upsilon_p = 196.5$ THz. Simulated field profiles of the valley kink state around the interface are displayed in Figure 2(b).

To visualize the topological protection of valley kink states in the VPCs, we perform the full-wave simulations to study the field distributions along the topological interface at the pump frequency $\upsilon_p = 196.5$ THz. We consider a "Z" shaped interface between the VPC_1 and VPC_2, as shown in Figure 2(d), we conduct an excitation $E_p = E_x + iE_y$ to emulate a right circularly polarized light. Note that valley-

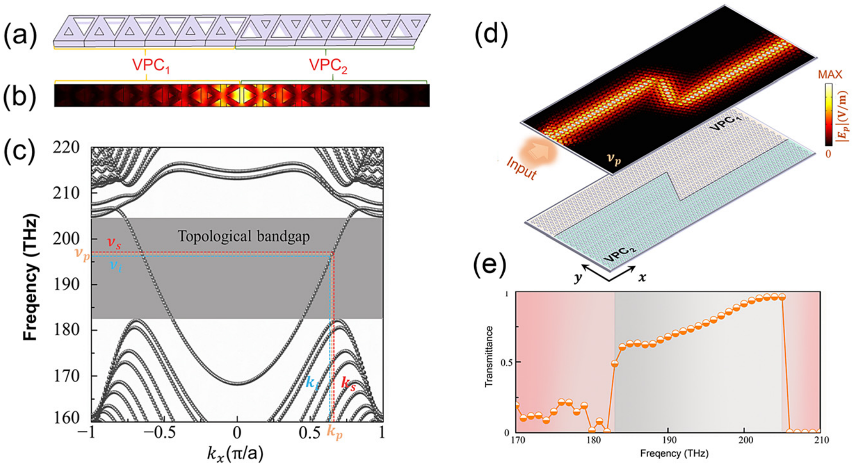

Figure 2: Topological valley kink states in photonic crystals emulating QVH effect.
(a) Schema of VPC structure comprising of VPC_1 and VPC_2. (b) Simulated field profiles of the valley kink state around the interface. (c) Calculated band diagram of valley kink states for VPC configuration, the gray region denotes the topological bandgap. (d) Field profiles of valley kink states along a "Z" shaped interface between the VPC_1 and VPC_2. (e) Linear transmittances of kink states, the light gray and pink regions represent the bandgap and bulk respectively.

polarized topological kink states are locked to the circular polarizations of the excited light, with right circularly polarized light locking to forward-propagating topological kink states, while left circularly polarized light locking to back-propagating kink states. The simulation result reveals that electromagnetic wave smoothly flows through sharp corners without visible back-scattering, which proves that kink states are robust against sharp bends due to the nature of topological protection. The vortex-like characteristic of excitation only supports one forward-propagating mode. Therefore, the backward-propagating mode is suppressed in the QVH system, which is analogous to the pseudospins of helical edge states in the QSH system [6, 7]. Remarkably, the electric field of the topological valley kink state is confined at the interface between two different VPCs.

We further explore the transmission spectrum of proposed VPCs with a "*Z*" shaped interface, as depicted in Figure 2(e). The detector dipoles are set around the input and output port. There exists a distinct peak between 183 and 205 THz, which is consistent with the bandwidth of the topological bandgap in the dispersion relations. The maximum transmittance is nearly unit in the bandgap; however, a sharp decline of transmittance appears for the bulk modes due to the reflection and scattering losses. It is worth mentioning that bulk modes are excited at the corner of the "*Z*" shape interface for the kink states at the low-frequency range, leading to undesired loss at the bends. Therefore, the transmittance of kink states is not unit at the low-frequency range. With the frequency increasing, the bulk modes cannot be excited because the frequency of kink states is far away from the frequency of bulk modes corresponding to the dispersion relations, which leads to the improvement of transmittance.

2.3 Entangled photon pairs of kink states

The spontaneous FWM is an efficient nonlinear process for the generation of entangled signal and idler photons. The occurrence of the FWM process is dictated by energy and momentum conversion, satisfying $2\omega_p = \omega_s + \omega_i$ and $2\boldsymbol{k}_p = \boldsymbol{k}_s + \boldsymbol{k}_i$, where $\boldsymbol{k}_p$, $\boldsymbol{k}_s$, and $\boldsymbol{k}_i$ are the wavevectors of pump, signal, and idler, respectively. With the overlap between the frequencies of FWM interactions and operation bandwidths of topological insulators, topological protection of correlated biphotons [22] in addition to frequency-entangled photon pairs [25] could be implemented. The dispersion relation of proposed VPCs illustrated in Figure 2(c) reveals that the dispersion slope is virtually linear, and there only exists one edge mode bounded to the valley. The dispersion relation provides a potential possibility to manipulate a broadband FWM process inside the topological bandgap; however, the phase-matching condition should be a major consideration for enhancing the FWM interaction. In particular, the energy conversion becomes more efficient when the nonlinear wavevector mismatch ($\Delta\boldsymbol{k} = 2\boldsymbol{k}_p - \boldsymbol{k}_s - \boldsymbol{k}_i$) satisfies $\Delta k = 0$. By utilizing the energy conversion of FWM interactions, we calculate the map of wavevector mismatch Δk of the VPC, as depicted in Figure 3(a). It is noted that the conversion efficiency of the FWM interaction increases as the wavevector mismatch Δk decreases. To get the small value of wavevector mismatch Δk of the map, we choose the frequencies of the nonlinear process as $\upsilon_p = 196.5$, $\upsilon_s = 196.9$, and $\upsilon_i = 196.1$ THz, respectively. The scalar nonlinear wavevector mismatch of this FWM process is calculated as $\Delta k = 1.89 \times 10^{-6}$.

To excite the nonlinear FWM interaction, the input field amplitudes of the pump and signal are set as $|E_p| = 4 \times 10^5$ and $|E_s| = 4 \times 10^4$ V/m, respectively. The excitation of the idler is replaced by scattering boundary condition, which implies that the input power of the idler is set as $|E_i| = 0$ V/m. The nonlinearity of silicon is considered as a third-order susceptibility tensor $\chi^{(3)}$ with a constant scalar value of 2.45×10^{-19} m^2/V^2.

Let us consider the evolution of the FWM process in the designed VPC. Field profiles of the signal and idler are simulated, and the results are depicted in Figure 3(b). It can be observed that a topological valley kink state of idler

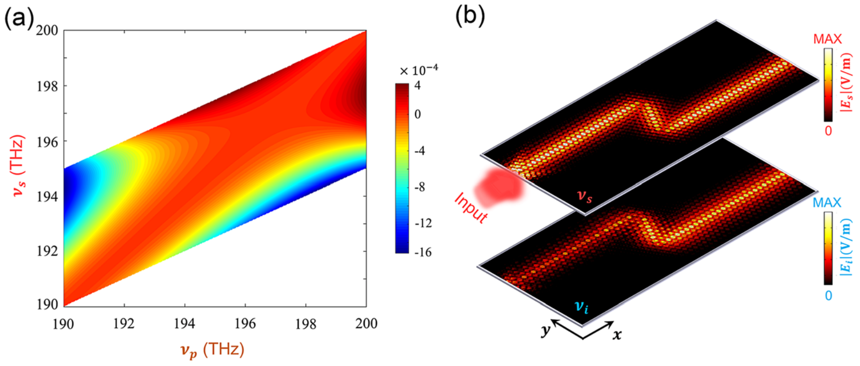

Figure 3: Topologically protected FWM interaction of valley kink states. (a) Map of wavevector mismatch Δk of the VPC, where ν_p, ν_s, and ν_i represent the frequency of pump, signal, and idler, respectively. (b) Field profiles of the signal ($\nu_s = 196.9$ THz) and idler ($\nu_i = 196.1$ THz) along the topological interface.

frequency is excited along the interface between two different VPCs, which gives evidence to the generation of the FWM process. Remarkably, there is no excitation at the frequency of the idler, therefore the field amplitudes of edge state at the input are almost invisible, and getting bigger with the propagation in the VPCs. Moreover, the valley kink state of generated idler photons is robust to the sharp bend, resulting in topological protection of idler photons due to the spectral overlap of the idler and edge states.

To theoretically calculate the continuous frequency entanglement of photon pairs emerging from the FWM process, we conduct the quantum evolvement of photon pairs (see Supplementary Material). The biphoton state generated form nonlinear FWM interaction can be written as

$$|\Psi\rangle = \iint d\omega_s d\omega_i \mathcal{A}(\omega_s,\omega_i)\hat{a}^{\dagger}_{\omega_s}\hat{a}^{\dagger}_{\omega_i}|0\rangle, \tag{1}$$

where $\hat{a}^{\dagger}_{\omega_s}$ and $\hat{a}^{\dagger}_{\omega_i}$ are creation operators, and $\mathcal{A}(\omega_s,\omega_i)$ is the JSA. Consider the phase-matching condition of FWM processes, the joint JSA is given by [27]

$$\mathcal{A}\,(\omega_s,\omega_i) = \alpha\left(\frac{\omega_s+\omega_i}{2}\right)\Phi(\omega_s,\omega_i), \tag{2}$$

where the spectrum envelope of the pump $\alpha\left(\frac{\omega_s+\omega_i}{2}\right)$ and joint phase-matching spectrum $\Phi\,(\omega_s,\ \omega_i)$ are modeled approximately, with the forms of $\alpha\left(\frac{\omega_s+\omega_i}{2}\right) = \delta(\omega_s+\omega_i-2\omega_p)$ and $\Phi(\omega_s,\omega_i) = \mathrm{sinc}\left(\frac{\Delta kL}{2}\right)$. The JSA describing the biphoton state amplitude function in VPCs is depicted in Figure 4(a), gives a moderate probability of entanglement between signal and idler photons. To quantify this, the Schmidt decomposition method is employed to testify the separability of the JSA.

The normalized Schmit coefficients λ_n represents the probability of obtaining the nth biphoton state. As shown in Figure 4(b), the number of nonzero Schmit coefficients λ_n is greater than 1, leading to clear evidence of entanglement of biphotons. The entanglement can also be described by the entropy of entanglement [27] with $S_k > 0$, where $S_k = -\sum_{n=1}^{N}\lambda_n \log_2 \lambda_n$. The inset of Figure 4(b) demonstrates that the convergency value of entropy of entanglement is 6.49, which implies high quality of continuous frequency entanglement of biphotons in the VPCs. Furthermore, the emergence of valley kink states gives rise to the topological protection of entangled photon pairs originating from the FWM process in the VPCs.

3 Discussion

3.1 Entangled photon pairs in VPCs with different interfaces

Carefully considering the topological behaviors of VPCs with different interfaces, we construct a photonic crystal configuration with modulating inversely the localizations of VPCs, as shown in Figure 5(a). We perform an extensive calculation on the dispersion relation of designed VPCs. As depicted in Figure 5(c), there exists a dispersion curve distinguished from the bulk inside the bandgap, which denotes the topological one-way edge modes along the interface. Comparing with the dispersion relation of VPCs with the first type interface (shown in Figure 2(c)), the slopes of dispersion curves of VPCs with the second type interface exhibit opposite values owing to inversion of lattice symmetry for VPCs. It is worth mentioning that bands of kink edge states in two interfaces are not perfect mirror-symmetric, which is contributed by the unrighteous symmetry of unit cells of VPCs ($d_1 \neq d_2$). We simulate the field profiles of valley kink states around the interface as illustrated in Figure 5(b). Analogously, the map of wavevector mismatch Δk in the VPC is calculated as depicted in Figure 5(d). Compared with the map of wavevector

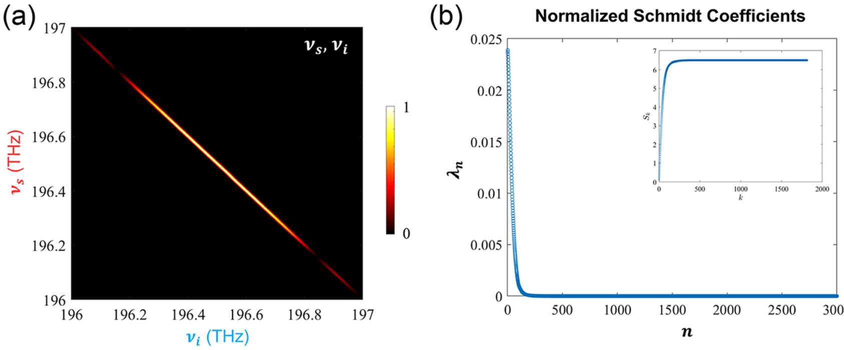

Figure 4: Quantum characteristics of photon pairs in the VPCswith the first type interface.
(a) JSA distribution of the signal and idler in the VPCs comprising of VPC_1 and VPC_2.
(b) Normalized Schmidt coefficients of photon pairs after propagation along the topological interface, the inset shows the entropy of entanglement of the system.

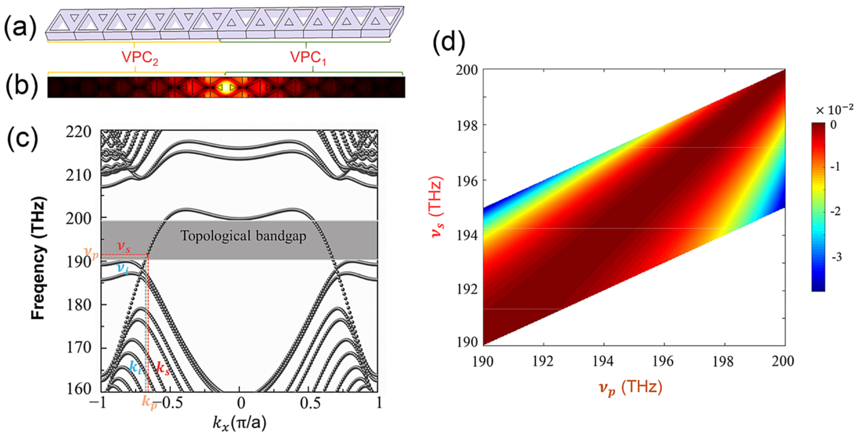

Figure 5: Topological valley kink states in VPCs with different interfaces.
(a) Schema of proposed VPC structure comprising of VPC$_2$ and VPC$_1$. (b) Simulated field profiles of the valley kink state around the interface. (c) Calculated band diagram of valley kink states in the designed VPC. (d) Map of wavevector mismatch Δk of the VPC.

mismatch Δk in the VPC shown in Figure 3(a), the relative values of wavevector mismatch Δk are larger, resulting in the lower efficiency of conversion of the FWM interaction.

We study the spontaneous FWM interaction in designed VPCs with different interfaces, the frequencies of the pump, signal and idler are chosen as υ_p = 191.8, υ_s = 191.9 and υ_i = 191.7 THz, respectively. The scalar nonlinear wavevector mismatch is calculated as $\Delta k = -8.42 \times 10^{-6}$. We perform the numerical simulations of nonlinear FWM interactions along a "*Z*" shaped interface between the VPC$_2$ and VPC$_1$, the field profiles of the pump along the interface are depicted in Figure 6(a). The field profiles of the signal and idler are shown in Figure 6(b), idler photons are generated and amplified with the light propagation of edge states as a result of the emergence of the nonlinear FWM process. The valley kink states of pump, signal, and idler propagating along the interface between VPC$_2$ and VPC$_1$ are robust to the sharp bends.

According to the map of wavevector mismatch Δk of designed VPCs, we draw the JSA of biphoton state propagating along the interface between the VPC$_2$ and VPC$_1$. As illustrated in Figure 7(a), the joint spectrum intensity implies that the frequency correlation of the signal and idler is not strong. Large values of relative wavevector mismatch Δk lead to low efficiency of the FWM process. Analogously, the entanglement of biphotons in the VPCs comprising of

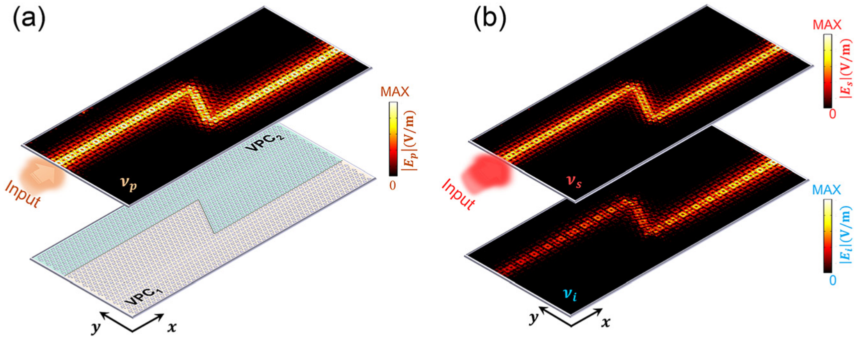

Figure 6: FWM interactions in VPCs with different interfaces.
(a) Field profiles of the pump (ν_p = 190.8 THz) along a "*Z*" shaped interface between the VPC$_2$ and VPC$_1$. (b) Field profiles of the signal (ν_s = 190.9 THz) and idler (ν_i = 190.7 THz) in the VPCs.

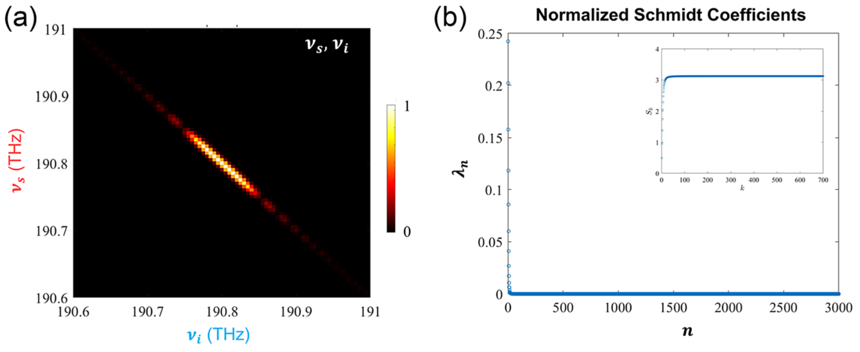

Figure 7: Quantum characteristics of photon pairs in the VPCs with the second type interface.
(a) JSA distribution of the signal and idler.
(b) Normalized Schmidt coefficients of biphoton states after propagation along the topological interface, the inset shows the entropy of entanglement of the system.

VPC_2 and VPC_1 is clarified. The normalized Schmidt coefficients λ_n of biphotons is depicted in Figure 7(b), which reveals that the biphoton state is entangled. However, comparing with the results of VPCs with the first type interface (shown in Figure 4), the number of nonzero Schmit coefficients λ_n is small, indicating the low quality of entanglement between signal and idler photons. The wavevector mismatch Δk of the second type of VPC interface is two orders of magnitude higher than that of the first type of VPC interface shown in Figure 3(a), which implies that few FWM processes satisfying the phase-matching condition emerge for the second type of VPC interface. It can also be proved by bandwidth of the JSA distribution of two VPCs. For the second type of VPC interface, the dimensions of JSA $\mathcal{A}(\omega_s, \omega_i)$ in Hilbert space are lower, therefore, the number of nonzero Schmit coefficients λ_n is smaller, resulting in lower quality of entanglement. The result is also proved by the entropy of entanglement S_k plotted in the inset of Figure 7(b).

4 Conclusions

In this work, we have demonstrated a photonic-crystal-based platform that combines the topological photonic systems and entangled biphoton states. In particular, the topological valley kink states propagating along the interfaces are observed in photonic crystals emulating the QVH effect. Simulated transmittances of kink states confirm the behaviors of topological properties, including back-scattering suppression and immunity to structure imperfections. By introducing the nonlinear FWM interaction into photonic systems, we conduct the generation and amplification of idler photons along the interfaces between two different VPCs. We theoretically clarify that the photon pairs generated from the FWM interaction are continuous frequency entangled. Moreover, with the overlap between the frequencies of FWM interactions and operation bandwidths of valley kink states, the one-way propagating modes of the pump, signal and idler show robustness against the sharp bends and scattering, giving rise to the topological protection of entangled photon pairs.

5 Methods

5.1 Numerical modeling

We use the finite-element method solver COMSOL Multiphysics to conduct numerical simulations of topological photonic crystals. The material of photonic crystals is chosen as silicon due to the extensive application and high third-order nonlinearity $\chi^{(3)}$. For simplified calculation, the refractive index of silicon is performed as $n_{Si} = 2.965$ in two-dimensional configuration [16, 28]. We also prove that topological protected entangled photon pairs can be achieved even consider the material dispersion of silicon.

In this case, we consider the topological behavior of transverse electric polarization modes in the VPCs. We have simulated the field profiles of topological valley kink states in the VPCs with a source $E_p = E_x + iE_y$ that emulates a right circularly polarized light. The circular polarizations of the source are analogous to the pseudospins in the QSH systems [6, 29–32]. Two detector dipoles are set around the input and output port along the "Z" shaped interface to calculate the transmittances of kink states.

To perform the nonlinear elements in the VPCs, the third-order nonlinearity of silicon $\chi^{(3)}$ is identified by a constant scalar value [33] of 2.45×10^{-19} m^2/V^2. The FWM interaction is conducted by the third-order nonlinear polarization of silicon, which is described by

$$\boldsymbol{P}_p(\omega_s + \omega_i - \omega_p) = 6\epsilon_0 \chi^{(3)} \boldsymbol{E}_s \boldsymbol{E}_i \boldsymbol{E}_p^*, \tag{3}$$

$$\boldsymbol{P}_s(\omega_p + \omega_p - \omega_i) = 6\epsilon_0 \chi^{(3)} \boldsymbol{E}_p \boldsymbol{E}_p \boldsymbol{E}_i^*, \tag{4}$$

$$\boldsymbol{P}_i(\omega_p + \omega_p - \omega_s) = 6\epsilon_0 \chi^{(3)} \boldsymbol{E}_p \boldsymbol{E}_p \boldsymbol{E}_s^*, \tag{5}$$

where $\boldsymbol{P}_{p,\ s,\ i}$ and $\boldsymbol{E}_{p,\ s,\ i}$ are the polarization and electric field of the pump, signal, and idler. In the simulations, the input field amplitudes of the pump and signal are set as $|E_p| = 4 \times 10^5$ and $|E_s| = 4 \times 10^4$ V/m, respectively. The input electric field amplitude of the idler is set as $|E_i| = 0$ V/m, then the excitation of model at the idler frequency is driven by the nonlinear coupling of electromagnetic models at the pump and signal frequencies. Therefore, the generation of edge modes at the idler frequency implies the emergence of the nonlinear FWM interaction.

5.2 Hamiltonian of FWM interaction

The nonlinear FWM interaction is generated in the VPCs due to the third-order nonlinearity of silicon $\chi^{(3)}$. It is noted that the Hamiltonian governing FWM interaction is described by

$$H = H_L + H_{NL}, \tag{6}$$

where [20, 21, 34]

$$H_L = \sum_j \int d\omega_j \hbar \omega_j a^\dagger_{j,\omega_j} a_{j,\omega_j}, \tag{7}$$

$$H_{NL} = -\gamma_0 \int d\omega_p d\omega_s d\omega_i a^\dagger_{p,\omega_p} a^\dagger_{p,\omega_p} a_{s,\omega_s} a_{i,\omega_i} e^{i(2k_p - k_s - k_i)x} + h.c., \tag{8}$$

with γ_0 is effective nonlinear coupling constant, $a^\dagger_\mu$ is the creation operator of the pump, signal and idler photons represented by $\mu \in \{p, s, i\}$.

Author contributions: All the authors have accepted responsibility for the entire content of this submitted manuscript and approved submission.

Research funding: This work is supported by the Key-Area Research and Development Program of Guangdong Province (2018B030325002) and the National Natural Science Foundation of China (62075129, 61975119).

Conflict of interest statement: The authors declare that they have no conflict of interest.

References

[1] F. Haldane and S. Raghu, “Possible realization of directional optical waveguides in photonic crystals with broken time-reversal symmetry,” *Phys. Rev. Lett.*, vol. 100, 2008, Art no. 013904.

[2] S. Raghu and F. D. M. Haldane, “Analogs of quantum-Hall-effect edge states in photonic crystals,” *Phys. Rev. A*, vol. 78, 2008, Art no. 033834.

[3] M. Hafezi, S. Mittal, J. Fan, A. Migdall, and J. Taylor, “Imaging topological edge states in silicon photonics,” *Nat. Photon.*, vol. 7, pp. 1001–1005, 2013.

[4] A. Slobozhanyuk, S. H. Mousavi, X. Ni, et al., “Three-dimensional all-dielectric photonic topological insulator,” *Nat. Photon.*, vol. 11, pp. 130–136, 2017.

[5] X. Cheng, C. Jouvaud, X. Ni, et al., “Robust reconfigurable electromagnetic pathways within a photonic topological insulator,” *Nat. Mater.*, vol. 15, pp. 542–548, 2016.

[6] L.-H. Wu and X. Hu, “Scheme for achieving a topological photonic crystal by using dielectric material,” *Phys. Rev. Lett.*, vol. 114, p. 223901, 2015.

[7] M. A. Gorlach, X. Ni, D. A. Smirnova, et al., “Far-field probing of leaky topological states in all-dielectric metasurfaces,” *Nat. Commun.*, vol. 9, pp. 1–8, 2018.

[8] N. Parappurath, F. Alpeggiani, L. Kuipers, and E. Verhagen, “Direct observation of topological edge states in silicon photonic crystals: spin, dispersion, and chiral routing,” *Sci. Adv.*, vol. 6, p. eaaw4137, 2020.

[9] F. Gao, H. Xue, Z. Yang, et al., “Topologically protected refraction of robust kink states in valley photonic crystals,” *Nat. Phys.*, vol. 14, pp. 140–144, 2018.

[10] X.-T. He, E.-T. Liang, J.-J. Yuan, et al., “A silicon-on-insulator slab for topological valley transport,” *Nat. Commun.*, vol. 10, pp. 1–9, 2019.

[11] J.-W. Dong, X.-D. Chen, H. Zhu, Y. Wang, and X. Zhang, “Valley photonic crystals for control of spin and topology,” *Nat. Mater.*, vol. 16, pp. 298–302, 2017.

[12] X. Wu, Y. Meng, J. Tian, et al., “Direct observation of valley-polarized topological edge states in designer surface plasmon crystals,” *Nat. Commun.*, vol. 8, pp. 1–9, 2017.

[13] S. Arora, T. Bauer, R. Barczyk, E. Verhagen, and L. Kuipers, “Direct quantification of topological protection in symmetry-protected photonic edge states at telecom wavelengths,” *Light Sci. Appl.*, vol. 10, pp. 1–7, 2021.

[14] D. Smirnova, A. Tripathi, S. Kruk, et al., “Room-temperature lasing from nanophotonic topological cavities,” *Light Sci. Appl.*, vol. 9, pp. 1–8, 2020.

[15] Y. Yang, Y. Yamagami, X. Yu, et al., “Terahertz topological photonics for on-chip communication,” *Nat. Photon.*, vol. 14, pp. 446–451, 2020.

[16] M. I. Shalaev, W. Walasik, A. Tsukernik, Y. Xu, and N. M. Litchinitser, “Robust topologically protected transport in photonic crystals at telecommunication wavelengths,” *Nat. Nanotechnol.*, vol. 14, pp. 31–34, 2019.

[17] W. Noh, H. Nasari, H.-M. Kim, et al., “Experimental demonstration of single-mode topological valley-Hall lasing at telecommunication wavelength controlled by the degree of asymmetry,” *Opt. Lett.*, vol. 45, pp. 4108–4111, 2020.

[18] D. Smirnova, S. Kruk, D. Leykam, et al., “Third-harmonic generation in photonic topological metasurfaces,” *Phys. Rev. Lett.*, vol. 123, p. 103901, 2019.

[19] J. W. You, Z. Lan, and N. C. Panoiu, “Four-wave mixing of topological edge plasmons in graphene metasurfaces,” *Sci. Adv.*, vol. 6, p. eaaz3910, 2020.

[20] S. Mittal, E. A. Goldschmidt, and M. Hafezi, “A topological source of quantum light,” *Nature*, vol. 561, pp. 502–506, 2018.

[21] S. Barik, A. Karasahin, C. Flower, et al., “A topological quantum optics interface,” *Science*, vol. 359, pp. 666–668, 2018.

[22] A. Blanco-Redondo, B. Bell, D. Oren, B. J. Eggleton, and M. Segev, “Topological protection of biphoton states,” *Science*, vol. 362, pp. 568–571, 2018.

[23] Y. Wang, X.-L. Pang, Y.-H. Lu, et al., “Topological protection of two-photon quantum correlation on a photonic chip,” *Optica*, vol. 6, pp. 955–960, 2019.

[24] Y. Chen, X.-T. He, Y.-J. Cheng, et al., “Topologically protected valley-dependent quantum photonic circuits,” *Phys. Rev. Lett.*, vol. 126, p. 230503, 2021.

[25] M. Wang, C. Doyle, B. Bell, et al., “Topologically protected entangled photonic states,” *Nanophotonics*, vol. 8, pp. 1327–1335, 2019.

[26] L. Zhang, Y. Yang, M. He, et al., “Valley kink states and topological channel intersections in substrate-integrated photonic circuitry,” *Laser Photon. Rev.*, vol. 13, p. 1900159, 2019.

[27] C. Law, I. A. Walmsley, and J. Eberly, “Continuous frequency entanglement: effective finite Hilbert space and entropy control,” *Phys. Rev. Lett.*, vol. 84, p. 5304, 2000.

[28] M. Hammer and O. V. Ivanova, “Effective index approximations of photonic crystal slabs: a 2-to-1-D assessment,” *Opt. Quant. Electron.*, vol. 41, pp. 267–283, 2009.

[29] W. Liu, M. Hwang, Z. Ji, et al., “Z2 photonic topological insulators in the visible wavelength range for robust nanoscale photonics,” *Nano Lett.*, vol. 20, pp. 1329–1335, 2020.

[30] X. Ni, D. Purtseladze, D. A. Smirnova, et al., “Spin-and valley-polarized one-way Klein tunneling in photonic topological insulators,” *Sci. Adv.*, vol. 4, 2018, Art no. eaap8802.

[31] Z.-K. Shao, H.-Z. Chen, S. Wang, et al., “A high-performance topological bulk laser based on band-inversion-induced reflection,” *Nat. Nanotechnol.*, vol. 15, pp. 67–72, 2020.

[32] W. Liu, Z. Ji, Y. Wang, et al., “Generation of helical topological exciton-polaritons,” *Science*, vol. 370, pp. 600–604, 2020.

[33] L. Wang, S. Kruk, K. Koshelev, et al., “Nonlinear wavefront control with all-dielectric metasurfaces,” *Nano Lett.*, vol. 18, pp. 3978–3984, 2018.

[34] J. W. Silverstone, D. Bonneau, K. Ohira, et al., “On-chip quantum interference between silicon photon-pair sources,” *Nat. Photon.*, vol. 8, pp. 104–108, 2014.

Supplementary Material: The online version of this article offers supplementary material (https://doi.org/10.1515/nanoph-2021-0371).